International Journal of Minerals, Metallurgy and Materials
Volume 24, Number 6, June 2017, Page 646
DOI: 10.1007/s12613-017-1447-9

Comparative study on the corrosion behavior of X52, 3Cr, and 13Cr steel in an O_2–H_2O–CO_2 system: products, reaction kinetics, and pitting sensitivity

Bing-wei Luo, Jie Zhou, Peng-peng Bai, Shu-qi Zheng, Teng An, and Xiang-li Wen

Beijing Key Laboratory of Failure, Corrosion and Protection of Oil/Gas Facilities, Department of Materials Science and Engineering, China University of Petroleum, Beijing 102249, China

(Received: 17 November 2016; revised: 1 March 2017; accepted: 3 March 2017)

Abstract: The corrosion behaviors of X52, 3Cr low-alloy steel, and 13Cr stainless steel were investigated in an O_2–H_2O–CO_2 environment at various temperatures and O_2–CO_2 partial-pressure ratios. The results showed that the corrosion rates of X52, 3Cr, and 13Cr steels increased with increasing temperature. The corrosion rates slowly increased at temperatures less than 100°C and increased sharply when the temperature exceeded 100°C. In the absence of O_2, X52, 3Cr, and 13Cr exhibited uniform corrosion morphology and $FeCO_3$ was the main corrosion product. When O_2 was introduced into the system, various forms of Fe_2O_3 appeared on the surface of the samples. The Cr content strongly influenced the corrosion resistance. The 3Cr steel with a low Cr content was more sensitive to pitting than the X52 or 13Cr steel. Thus, pitting occurred on the surface of 3Cr when 1.25 MPa of O_2 was added; this phenomenon is related to the non-uniform distribution of Cr in 3Cr.

Keywords: corrosion; oxygen; carbon dioxide; iron carbonate; iron oxide; pitting sensitivity

1. Introduction

Corrosion by carbon dioxide (CO_2) is an important corrosion factor in oil and gas collection and transportation systems [1–3]. Corrosion-induced failure of corroded pipelines and structural components can cause considerable economic losses and environmental pollution.

CO_2 corrosion is complicated. Numerous factors, including temperature, pressure, and flow velocity, influence the process and products of corrosion. Dong *et al.* [4] tested N80 steel under different CO_2 corrosion conditions and found that the corrosion rate is significantly higher under flowing conditions than that under static conditions. Adding O_2 transforms the uniform corrosion of pure CO_2 into pitting corrosion and increases the corrosion rate. Zhang *et al.* [5] attributed these phenomena to the $FeCO_3$, Fe_2O_3, and Fe_3O_4 corrosion products that formed in an O_2–CO_2 environment; specifically, these products exhibit a weaker protective effect on the metal matrix than $FeCO_3$ [5]. Jiang *et al.* [6] reported that corrosion rate markedly increases beyond the critical flow velocity, whereas corrosion rate is almost steady below the critical flow velocity. Wang *et al.* [7] reported that the tensile strength and elongation to failure of X80 steel decrease significantly with increasing H_2S/CO_2 partial-pressure ratio and that the corrosion rate of X80 steel is affected by the CO_2 partial pressure. Wei *et al.* [8] reported that the corrosion rate of X70 under a supercritical CO_2 environment is higher than that under a low CO_2 partial pressure.

As previously mentioned, the corrosion type of steel under CO_2 conditions is affected by the addition of O_2. Some possible explanations for this phenomenon have been proposed in recent years. According to the hypothesis proposed by McIntire *et al.* [9], CO_2 catalyzes steel corrosion, which induces the transformation of the initially formed corrosion product to FeO(OH). John *et al.* [10] showed that dissolved O_2 affects the hydration rate of CO_2 and develops a surface that facilitates hydrogen evolution. Moreover, O_2 impurities likely increase the corrosion rate under CO_2 conditions as a result of the change of the corrosion products formed in the O_2–CO_2 environment.

The addition of elemental Cr substantially increases the corrosion resistance of steel in many environments because

Corresponding author: Shu-qi Zheng E-mail: zhengsq09@163.com; zhengsq@cup.edu.cn

of the compactness and anion-passing selectivity of the corrosion product film [11]; these characteristics prevent anions such as Cl^-, CO_3^{2-}, and HCO_3^- from penetrating the corrosion products, thus decreasing the anion concentration at the interface. Elemental Cr induces a transition of the corrosion product from the crystalline to the amorphous state, which results in a denser corrosion scale and decreased susceptibility to localized corrosion [12]. As previously mentioned, the corrosion behavior of steel in a CO_2 environment is affected by H_2O and O_2 impurities [13] and by the Cr content of the steel [14–15].

The primary goal of this study is to investigate the effect of Cr content of the steel on their corrosion behavior under high-temperature, high-pressure O_2–H_2O–CO_2 conditions. X52, 3Cr, and 13Cr steels, which are commonly used in the oil and gas industry in China, were selected as the research materials. Mass-loss tests, scanning electron microscopy (SEM), energy-dispersive X-ray spectroscopy (EDS), and X-ray diffraction (XRD) were used to investigate the effect of Cr content of the steel on their corrosion behavior under experimental conditions.

2. Experimental

The materials used in this study were commercial X52, 3Cr, and 13Cr steels. The chemical compositions of these materials are presented in Table 1. The samples were machined into standard specimen with sizes of 50 mm × 10 mm × 3 mm. The specimens were then ground with SiC paper to grade 2000# and polished with a 0.5-μm diamond paste to prevent surface roughness from affecting pitting corrosion [16–17]. Finally, the specimens were ultrasonically cleaned in acetone and ethanol and then carefully stored for corrosion tests.

Table 1. Chemical compositions of commercial X52, 3Cr, and 13Cr steels wt%

Material	C	Si	Mn	S	P	Cr	Ni	Mo	Others	Fe
X52	0.13	0.40	1.50	0.003	0.020	—	—	—	—	Bal.
3Cr	0.16	0.22	0.51	0.002	0.009	3.02	0.05	0.35	—	Bal.
13Cr	0.14	0.30	0.20	0.010	0.602	12.70	0.20	—	0.1 Cu	Bal.

An autoclave was used to simulate static corrosion under high temperatures and pressures. Prior to each experiment, a test solution of 5wt% NaCl was prepared using analytical-reagent-grade NaCl and deionized water. O_2 was removed from the solution by continuous ventilation with N_2 for longer than 2 h; N_2 was removed with CO_2. Finally, CO_2 and O_2 were aerated into the autoclave as specified in Table 2. The corrosion experiments were conducted for 7 d.

Table 2. Experimental conditions of X52, 3Cr, and 13Cr steel in high temperature and high pressure autoclave

No.	Solution	Temperature / °C	CO_2 pressure / MPa	O_2 pressure / MPa
1	5wt% NaCl	25	1.25	1.25
2	5wt% NaCl	60	1.25	1.25
3	5wt% NaCl	100	1.25	1.25
4	5wt% NaCl	140	1.25	1.25
5	5wt% NaCl	60	1.25	0
6	5wt% NaCl	60	1.25	0.125
7	5wt% NaCl	60	1.25	0.6

Mass-loss tests were performed according to standard ASTM G31 [18]. Prior to the corrosion tests, the specimens were weighed three times using a digital balance with a precision of 0.0001 g. After the corrosion tests, the specimens were removed and cleaned with distilled water and acetone. The samples were then dried and stored. The corrosion films were subsequently removed from the surface of the specimens in accordance with the chemical product clean-up method [19]. After the specimens had dried, their mass was measured again. The corrosion rate was calculated according to the following equation:

$$R = \frac{8.76\times10^4\times(M_1 - M_2)}{StD} \quad (1)$$

where R is the corrosion rate, mm/a; M_1 is the mass of the sample before the experiment, g; M_2 is the mass of the sample after the corrosion products were removed, g; S is the surface area of the sample, cm^2; D is the density of the sample, g/cm^3; and t is the experiment time, h.

The characteristics of the corrosion products were established by SEM–EDS. XRD was used to accurately measure the structures of the corrosion products. The morphology of the samples was observed by SEM (FEI Quanta 200F). EDS analysis was performed using a Quanta 200F SEM coupled with a Trident XM4-type spectrometer. The X-ray diffractometer was a Bruker D8 Focus. The following parameters were applied for XRD analysis: X-ray source for Cu target; voltage current = 20 mA; scan angle 5°–90°; and scanning speed, 4°/min.

3. Results and discussion

The microstructures of the three tested materials are shown in Fig. 1. X52 consists of ferrite and pearlite, 3Cr consists of bainite, and 13Cr consists of martensite. The samples are important engineering materials that combine excellent mechanical properties and corrosion resistance. However, the samples showed disparate corrosion resistance in an O_2–CO_2 environment.

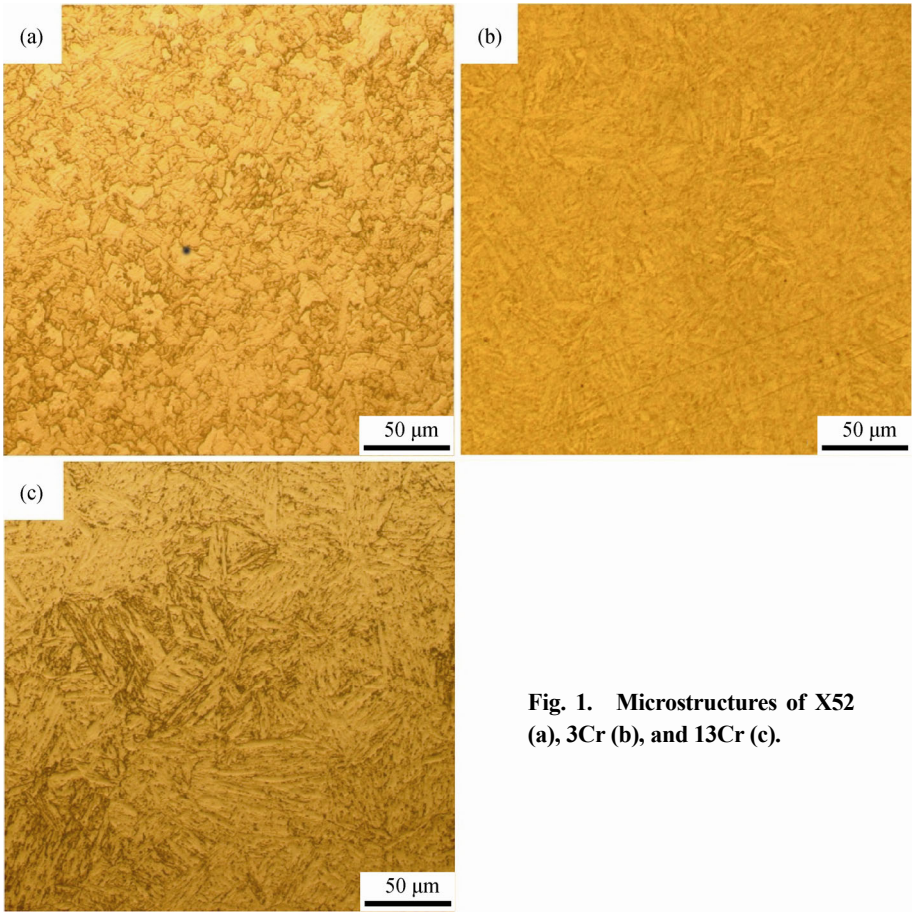

Fig. 1. Microstructures of X52 (a), 3Cr (b), and 13Cr (c).

Fig. 2 shows the morphology of specimens after the corrosion tests. The images were captured immediately after the specimens were removed from the autoclave to avoid oxidation. The experimental results show that X52 exhibited the worst corrosion resistance to the O_2–CO_2 environment, followed by 3Cr. The 13Cr steel showed the best corrosion resistance. However, this phenomenon was not observed at 140°C. At 140°C, the three materials did not exhibit distinctly different corrosion resistances. Therefore, the corrosion degree of the three materials increased with increasing temperature. Figs. 2(m)–2(o) shows that the corrosion products of the three materials were black in color. Some dark-red corrosion products were found on the specimens after a small amount of O_2 was added to the test environment (Figs. 2(p)–2(r)).

Fig. 3(a) shows that cubic ferrous carbonate ($FeCO_3$) is the corrosion product of X52 in the O_2–CO_2 environment at room temperature. As the temperature was increased, the corrosion products became more complex; flower-shaped corrosion products, which were only composed of Fe and O, were found and are shown in Fig. 4. Figs. 2 and 3 indicate that the 3Cr and 13Cr steels exhibit poor corrosion resistance at 140°C.

XRD was used to determine and characterize the phases in the corrosion products. Fig. 5 presents the XRD patterns of the corrosion products on the test specimens. Figs. 5(a)–5(d) shows that, as the test temperature was increased, the species of the corrosion products became increasingly convoluted. At 25°C, $FeCO_3$ (except for the Fe matrix) was only detected on the X52 specimens. This finding reveals that, at room temperature, only X52 suffered from CO_2 corrosion and that O_2 corrosion was negligible in this environment. At 60°C, X52 and 3Cr reacted with O_2 to form Fe_2O_3. When the temperature reached 100°C, $FeCO_3$ was not detected on the specimens. Compared with $FeCO_3$, Fe_2O_3 has a weaker protective effect on the metal matrix [6], which accounts for the high corrosion rate in this condition. The corrosion rate of 13Cr was lower than that of X52 and 3Cr at 100°C; additionally, Cr_2O_3 appeared on the surface of 13Cr. When the temperature was increased to 140°C, Fe_2O_3 and $FeCO_3$ appeared on the sample.

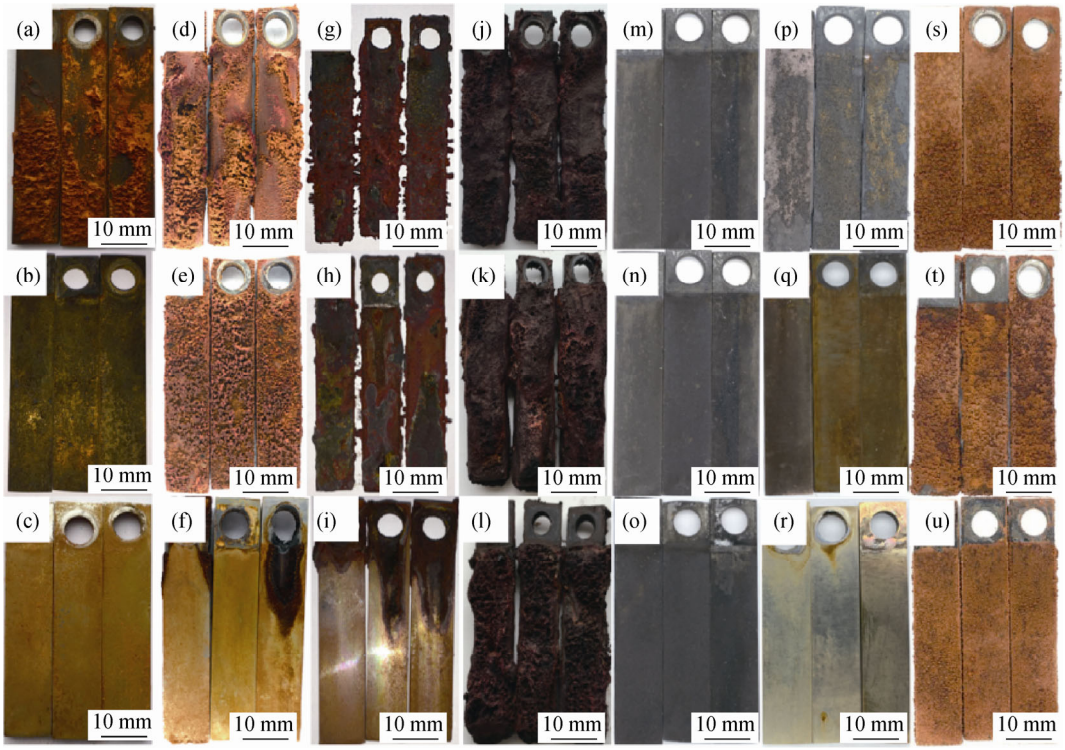

Fig. 2. Corrosion morphologies of different materials tested under different conditions shown in Table 2: (a–c) No. 1; (d–f) No. 2; (g–i) No. 3; (j–l) No. 4; (m–o) No. 5; (p–r) No. 6; (s–u) No. 7. The first, second, and third lines represent X52, 3Cr, and 13Cr, respectively.

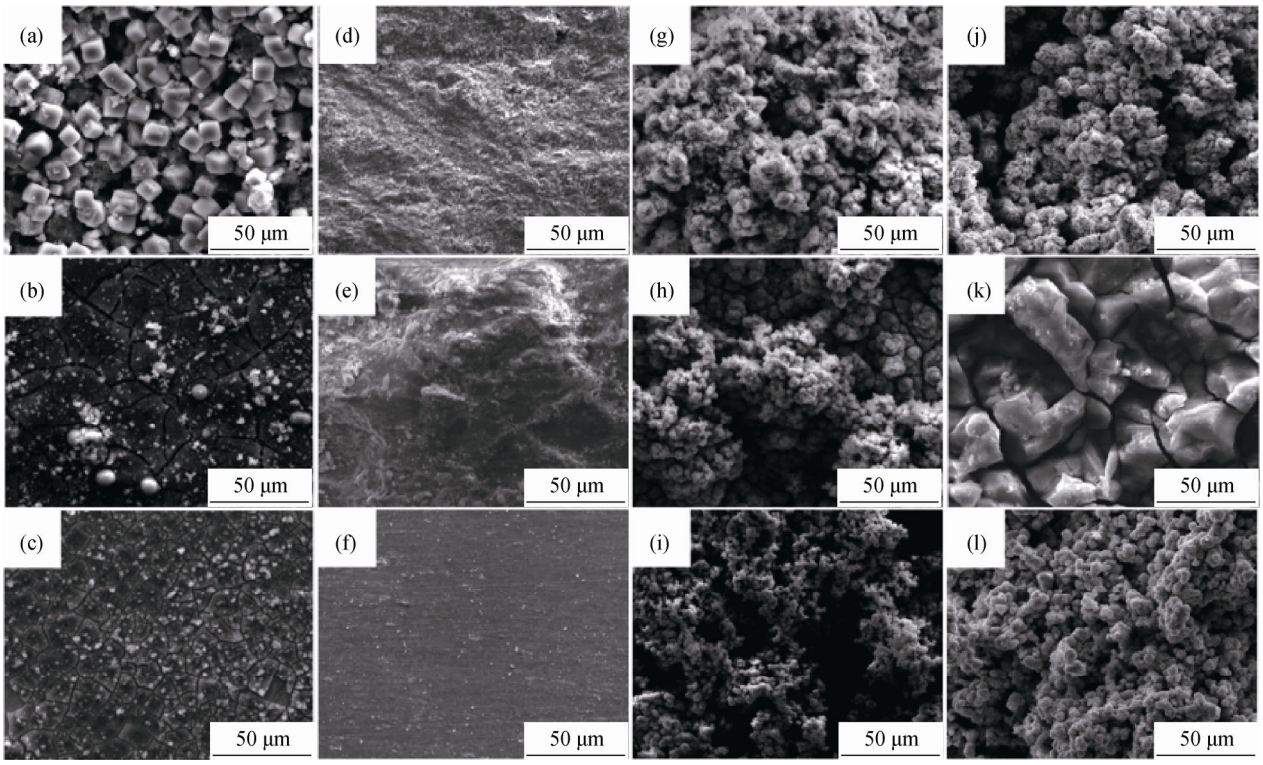

Fig. 3. Surface morphologies of the corrosion products of the tested materials: (a–c) No. 1; (d–f) No. 2; (g–i) No. 3; (j–l) No. 4. The first, second, and third lines represent X52, 3Cr, and 13Cr, respectively.

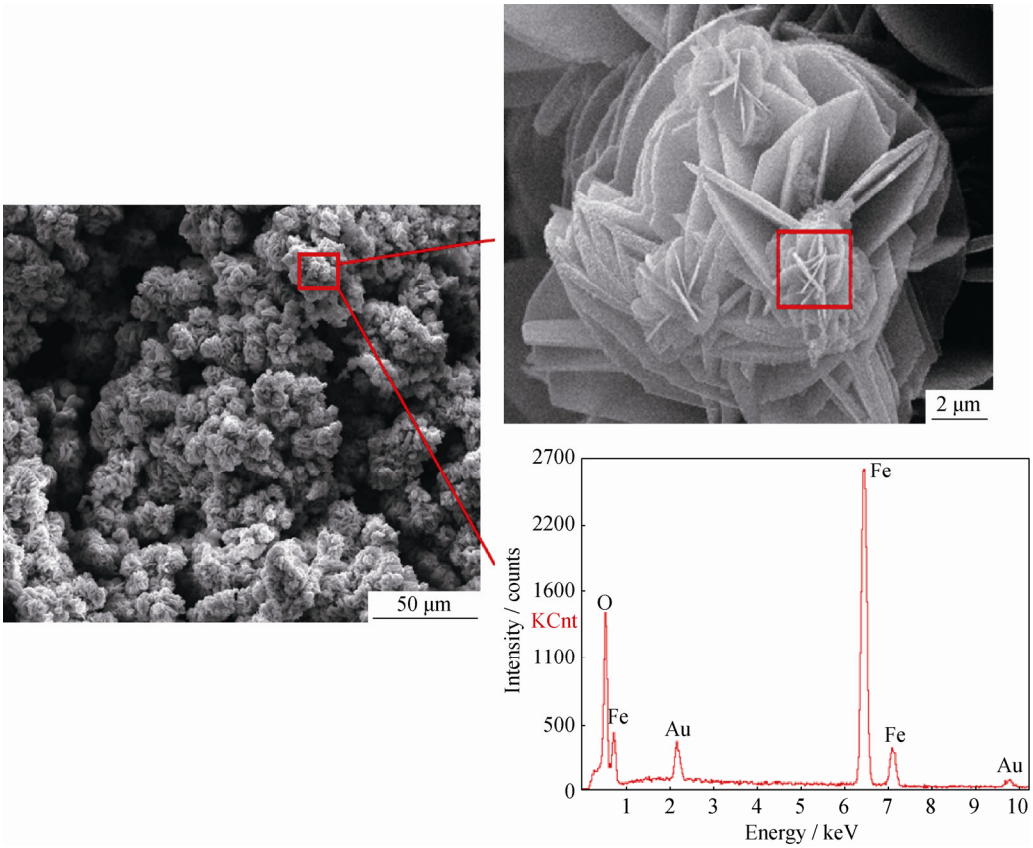

Fig. 4. EDS analysis of the flower-shaped corrosion product formed on the 3Cr specimen tested in No. 3 condition.

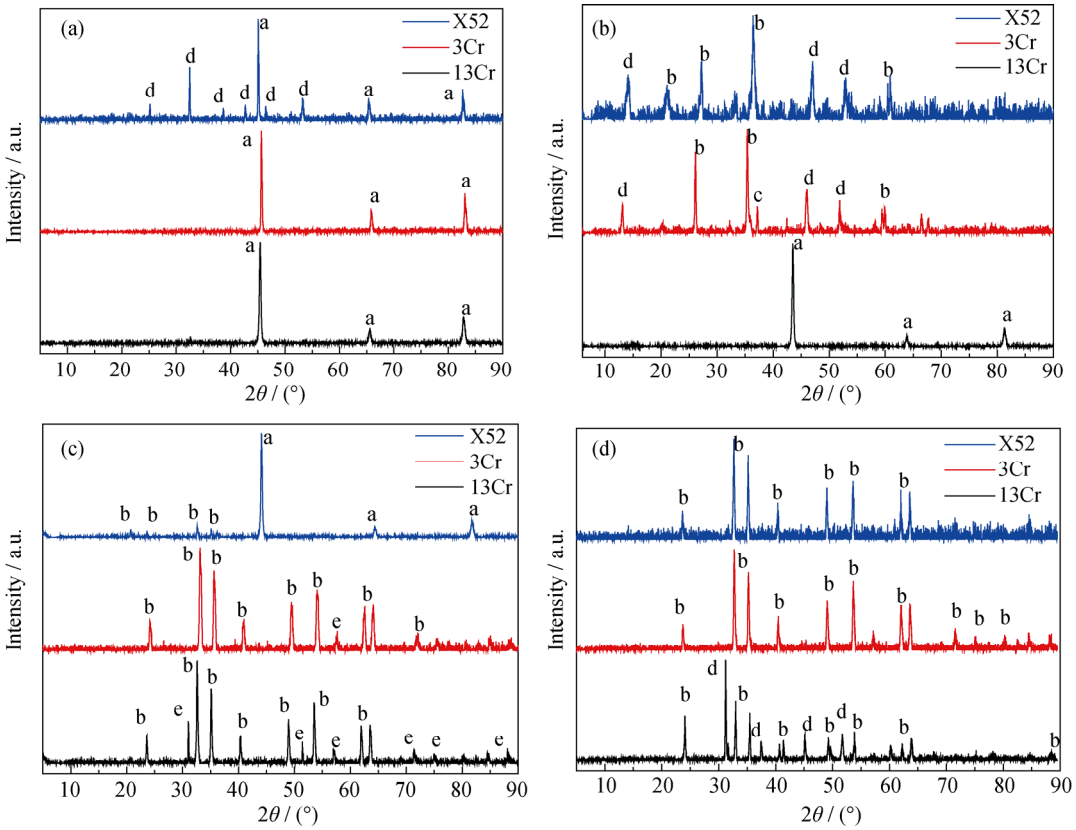

Fig. 5. XRD patterns of corrosion products formed at different test temperatures: (a) 25°C; (b) 60°C; (c) 100°C; (d) 140°C. The products are a—Fe, b—Fe_2O_3, c—Fe_3O_4, d—$FeCO_3$, e—Cr_2O_3, and f—FeO(OH).

The corrosion rates of the three tested materials at different temperatures were also determined from the cross-sectional morphology of the corrosion products, which are shown in Fig. 6. The corrosion products decreased with increasing Cr content, which indicated that elemental Cr is important for the corrosion resistance of steel in the O_2–CO_2 environment. As the temperature increased, the thickness of the corrosion products also increased. Compared with X52 (0wt% Cr) and 13Cr (13wt% Cr), 3Cr (3wt% Cr) was more sensitive to pitting corrosion at both 60 and 100°C. These temperatures resulted in pit depths of 26 and 30 μm on the surface of 3Cr. Uniform corrosion occurred at 25 and 140°C.

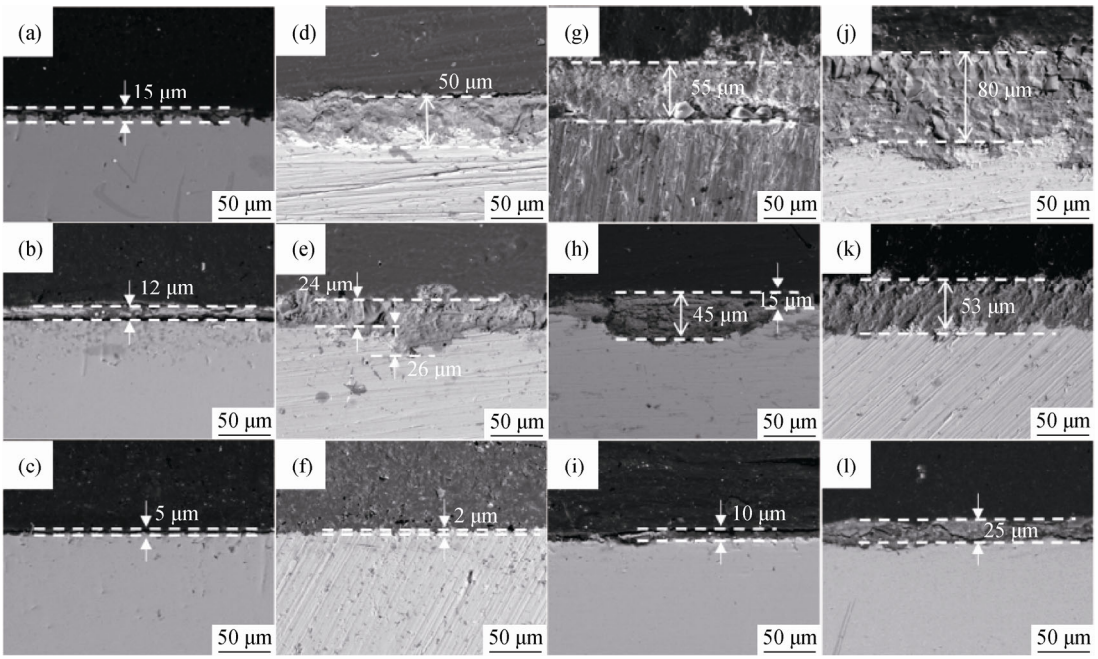

Fig. 6. Cross-sectional morphologies of the corrosion products: (a–c) No. 1; (d–f) No. 2; (g–i) No. 3; (j–l) No. 4. The first, second, and third lines represent X52, 3Cr, and 13Cr, respectively.

Corrosion rates were estimated in accordance with Eq. (1) above and are shown in Fig. 7. X52 exhibited the highest corrosion rate, and 13Cr had the lowest corrosion rate. Corrosion rates increased with increasing temperature, which is similar to the findings of Zhu *et al.* [20], who reported that the corrosion rate slowly increases at temperatures less than 100°C and significantly increases at temperatures greater than 100°C. The 3Cr steel exhibited a corrosion rate that was almost equal to that of X52 at 140°C . Moreover, at 140°C, the corrosion rate of 13Cr was lower than that of the other two samples.

Fig. 8 shows the surface morphologies of the corrosion products in O_2–CO_2 environments with different partial-pressure ratios. As shown in Figs. 8(a)–8(c), the $FeCO_3$ crystal is the main corrosion product. As the Cr content increased, however, the amount of corrosion product decreased substantially. The corrosion product of 3Cr, which is shown in Fig. 8(b), has a double-layer structure. According to Guo *et al.* [21], the inner layer is an amorphous structure that contains some nanoquasicrystalline and nanocrystalline grains; these grains are more uniform and less porous than the outer crystalline $FeCO_3$ layer. This structure provides more protection to the matrix than the single layer on X52. As shown in Figs. 8(d)–8(f), the corrosion product of Fe_2O_3 appeared as soon as O_2 was added to the test system. The corrosion product in Fig. 8(h) also shows a double-layer structure. Fig. 9 shows the energy spectra of this double-layer structure, which revealed that the inner layer contained elemental C. The

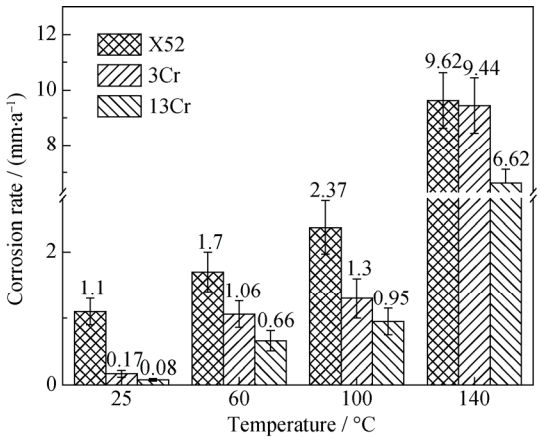

Fig. 7. Corrosion rates of X52, 3Cr, and 13Cr at different test temperatures; the error bars represent the maximum and minimum values.

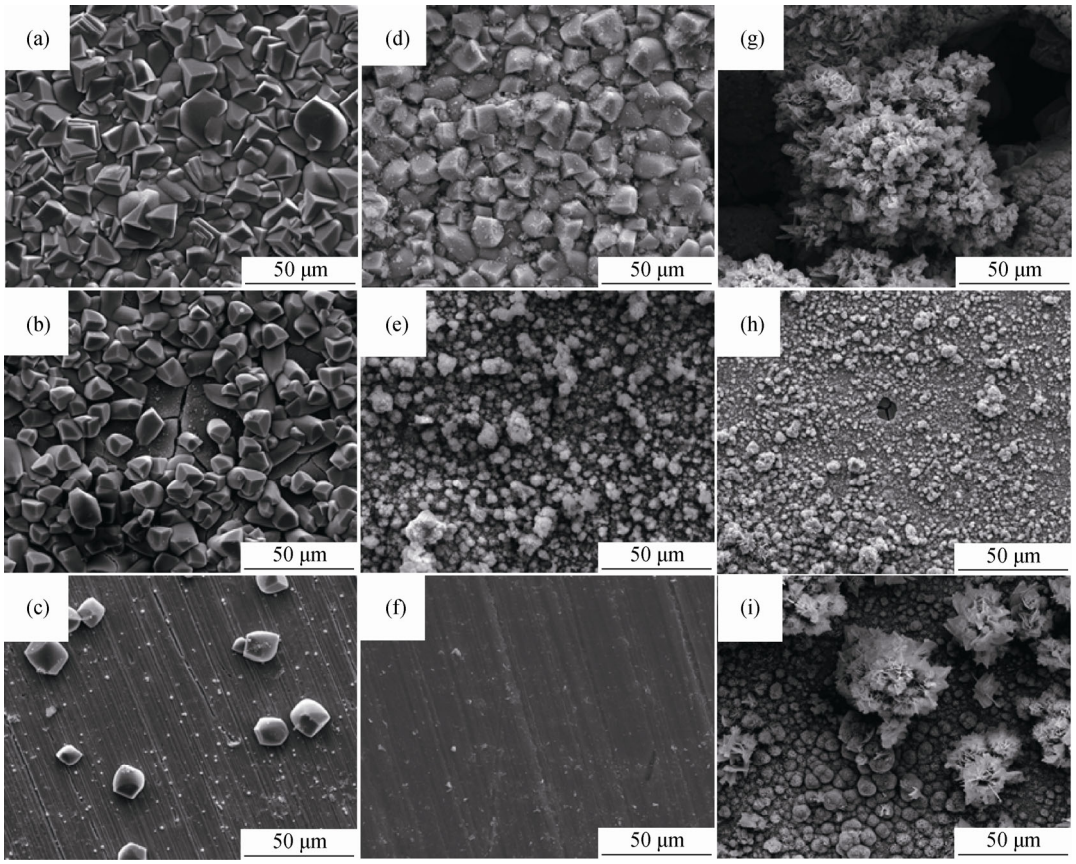

Fig. 8. Surface morphologies of corrosion products on the test materials: (a–c) No. 5; (d–f) No. 6; (g–i) No. 7. The first, second, and third lines represent X52, 3Cr, and 13Cr, respectively.

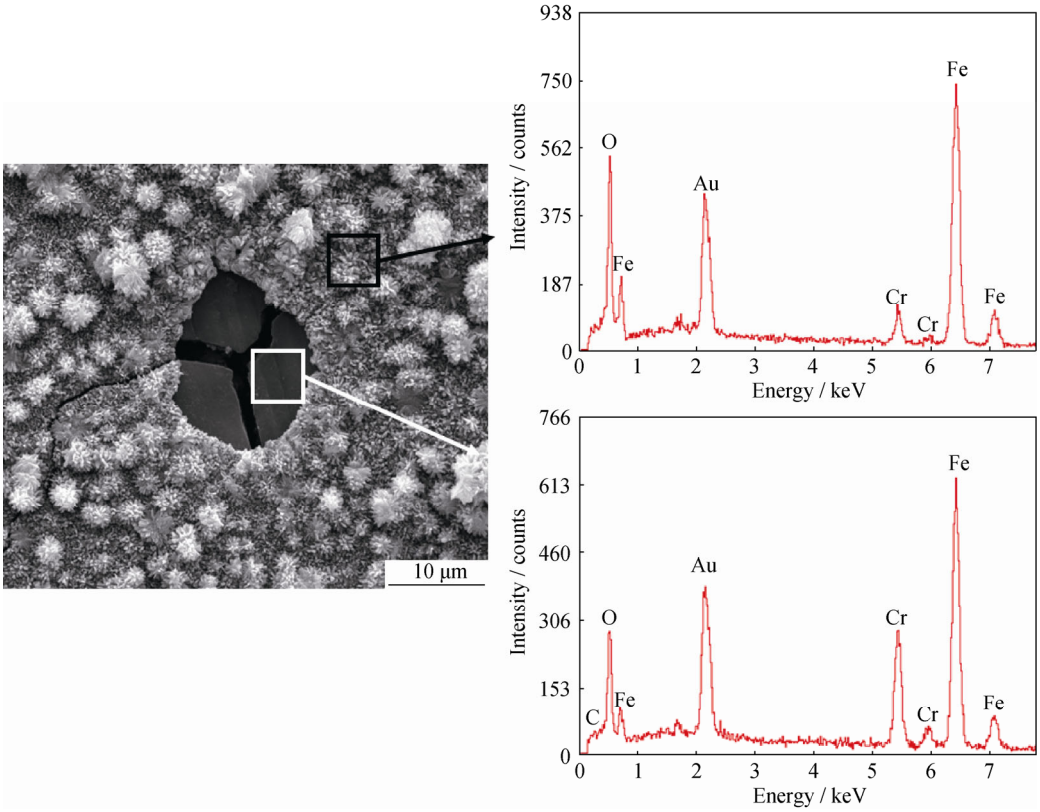

Fig. 9. EDS spectra of the double-layered corrosion products on the 3Cr specimen tested in No. 7 condition.

inner layer is likely composed mainly of $FeCO_3$, and that the outer layer is likely composed mainly of elemental Fe, O, and Cr. The composition of the layers indicates that the main corrosion products are iron oxides and Cr_2O_3.

Fig. 10 illustrates the XRD patterns of the corrosion product on the test specimens. The species of corrosion products became more complex as O_2 pressure increased. In the absence of O_2 in the environment in Fig. 10(a), $FeCO_3$ was mainly detected on the surfaces of X52 and 3Cr (except for the Fe matrix), which indicates that X52 and 3Cr were subjected to CO_2 corrosion. When the O_2 pressure was 0.125 or 0.6 MPa in Figs. 10(b)–10(c), Fe_2O_3 was mainly detected on the surfaces of X52, 3Cr, and 13Cr. Hence, O_2 corrosion dominated. When the O_2 pressure was further increased to 1.25 MPa in Fig. 5(b), Fe_2O_3 and $FeCO_3$ were mainly detected on the surfaces of X52 and 3Cr. Therefore, increasing the O_2 pressure not only changes the type of corrosion products but also exacerbates corrosion.

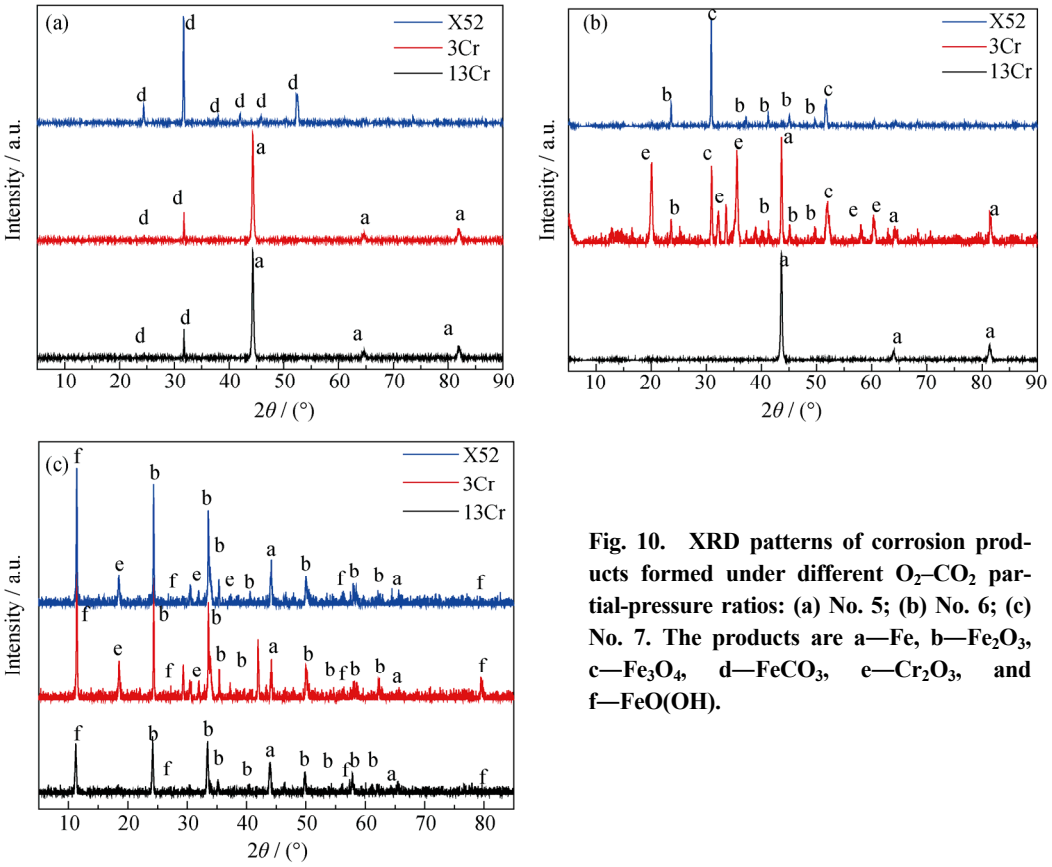

Fig. 10. XRD patterns of corrosion products formed under different O_2–CO_2 partial-pressure ratios: (a) No. 5; (b) No. 6; (c) No. 7. The products are a—Fe, b—Fe_2O_3, c—Fe_3O_4, d—$FeCO_3$, e—Cr_2O_3, and f—FeO(OH).

Fig.11 shows that the tendency of element Cr to decrease the thickness of the corrosion product remained the same, except in the case of 3Cr in the environment with an O_2 partial pressure of 0.6 MPa. However, the calculated value shows that the corrosion rate of 3Cr under similar conditions is low because of the loose structure of Fe_2O_3.

Fig. 12 shows the corrosion rate that was calculated from the mass-loss data. According to Zheng and Young [22], oxide growth on Fe–28Cr follows the parabolic law and the rate constant is independent of O_2 partial pressure at 900°C. However, the results of the present research show that, when the O_2 content increased and the O_2 pressure increased from 0 to 0.6 MPa, the corrosion rate of X52 increased from 0.74 to 3.11 mm/a. This phenomenon occurred because X52 is sensitive to O_2 when the O_2 pressure increases to a certain value. In the absence of O_2 in the system, the only corrosion product was $FeCO_3$, which protects the matrix from further damage. According to Zhang, the mixture of iron oxides and $FeCO_3$ has a weaker protective effect than $FeCO_3$ [5]; this finding was also supported by the surface morphologies shown in Fig. 8. As the O_2 content increased from 0.6 to 1.25 MPa, the corrosion rate of X52 decreased, this is because that the corrosion products generated at high O_2 pressure have a better protection.

The formation of $FeCO_3$ is in accordance with reaction (2) in the absence of O_2:

$$Fe^{2+} + CO_3^{2-} \rightarrow FeCO_3 \quad (2)$$

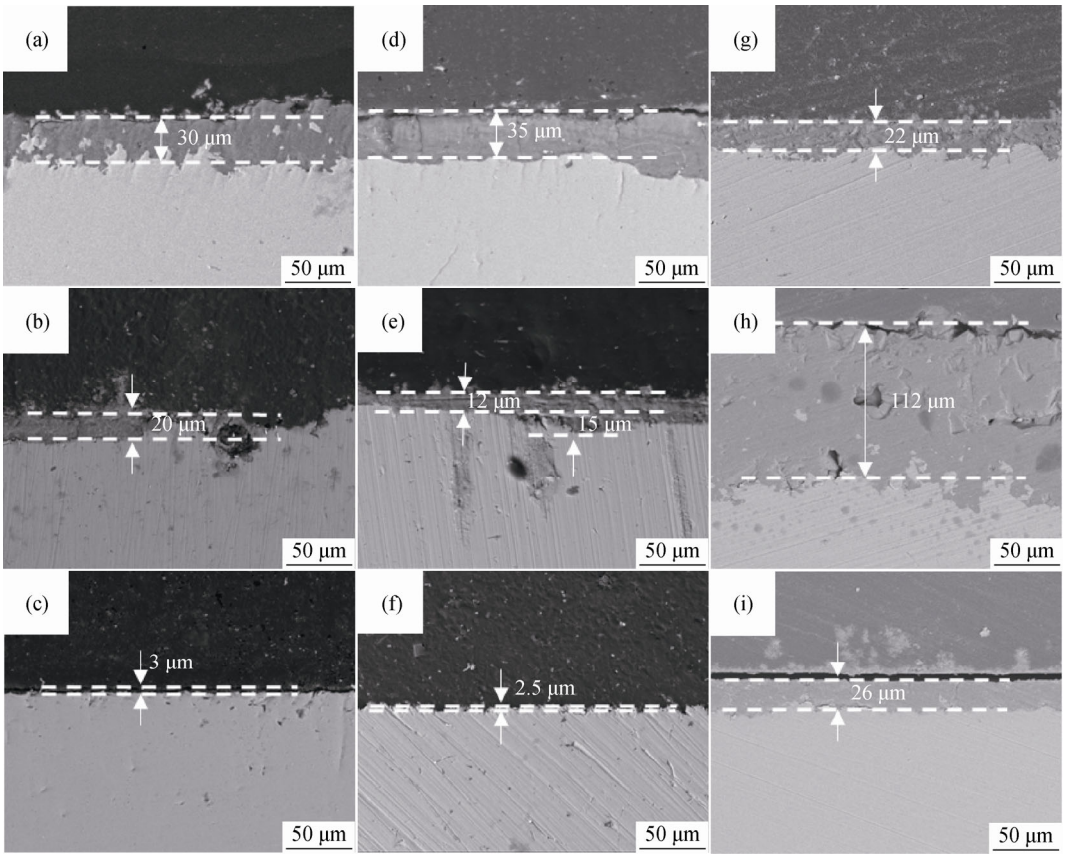

Fig. 11. Cross-sectional morphologies of the corrosion products: (a–c) No. 5; (d–f) No. 6; (g–i) No. 7. The first, second, and third lines represent X52, 3Cr, and 13Cr, respectively.

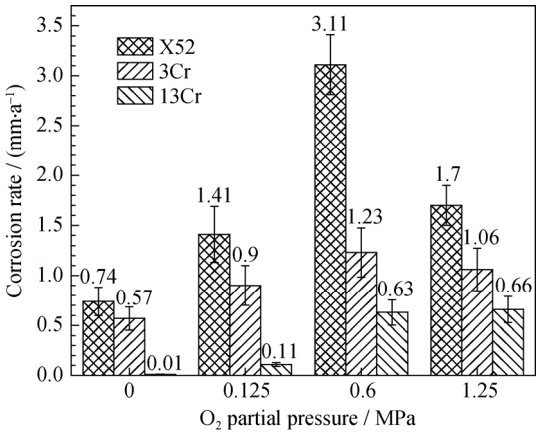

Fig. 12. Corrosion rates of X52, 3Cr, and 13Cr in different O_2 partial pressure environments; the error bar represents the maximum and minimum values.

In the presence of O_2, the cathodic reaction is:

$$O_2 + 2H_2O + 4e^- \rightarrow 4OH^- \quad (3)$$

According to Dong *et al.* [4], in the presence of O_2, the following reactions also occur:

$$4Fe^{2+} + 4H^+ + O_2 \rightarrow 4Fe^{3+} + 2H_2O \quad (4)$$

$$Fe^{3+} + 3H_2O \rightarrow Fe(OH)_3 + 3H^+ \quad (5)$$

$$Fe(OH)_3 \Leftrightarrow FeO(OH) + H_2O \quad (6)$$

$$2FeO(OH) \Leftrightarrow Fe_2O_3 + H_2O \quad (7)$$

$$8FeO(OH) + Fe \rightarrow 3Fe_3O_4 + 4H_2O \quad (8)$$

$$Fe^{2+} + 2H_2O \rightarrow Fe(OH)_2 + 2H^+ \quad (9)$$

$$4Fe(OH)_2 + O_2 + 2H_2O \rightarrow 4Fe(OH)_3 \quad (10)$$

$$4Fe_3O_4 + O_2 \rightarrow 6Fe_2O_3 \quad (11)$$

However, as shown in the XRD patterns, FeO(OH) was almost undetected in the corrosion products because of the relatively long experimental period of 7 d; FeO(OH) is unstable and is easily transformed to Fe_2O_3 or Fe_3O_4 according to reactions (7) or (8). In an environment with adequate O_2, Fe_3O_4 is easily transformed to Fe_2O_3, which accounts for the ubiquity of Fe_2O_3 in the XRD patterns.

4. Conclusions

(1) The corrosion rates of X52, 3Cr, and 13Cr increased with increasing test temperature. The corrosion rates increased slowly at temperatures below 100°C and then increased sharply at temperatures above 100°C.

(2) As the O_2 content increased, the corrosion rate of X52 quickly increased compared to that of 3Cr and 13Cr. However, when the O_2 pressure reached a certain value, the corrosion rate

of X52 decreased. The corrosion rates of 3Cr and 13Cr first increased when the O_2 content was less than 0.6 MPa and then remained stable when the O_2 content continuously increased.

(3) In the absence of O_2, the main corrosion product was $FeCO_3$, however, the corrosion products changed to Fe_2O_3, Fe_3O_4, and $FeCO_3$ after O_2 induced into the system. As the O_2 content increased, the corrosion rate of X52 quickly increased compared to that of 3Cr and 13Cr, and the type of corrosion products changed also.

(4) Compared with X52 and 13Cr, 3Cr was more sensitive to pitting corrosion. This sensitivity is likely related to the uneven Cr distribution in 3Cr.

Acknowledgments

This work was financially supported by the National Natural Science Foundation of China (No. 51671215), the Science Foundation of China University of Petroleum, Beijing (No. LLYJ-2011-41), and the Ph.D Basic Research Innovation Foundation of China University of Petroleum, Beijing (No. 2462016YXBS06).

References

[1] D.P. Li, L. Zhang, J.W. Yang, M.X. Lu, J.H. Ding, and M.L. Liu, Effect of H_2S concentration on the corrosion behavior of pipeline steel under the coexistence of H_2S and CO_2, *Int. J. Miner. Metall. Mater.*, 21(2014), No. 4, p. 388.

[2] L.N. Xu, J.Y. Zhu, M.X. Lu, L. Zhang, and W. Chang, Electrochemical impedance spectroscopy study on the corrosion of the weld zone of 3Cr steel welded joints in CO_2 environments, *Int. J. Miner. Metall. Mater.*, 22(2015), No. 5, p. 500.

[3] Q.Y. Liu, L.J. Mao, and S.W. Zhou, Effects of chloride content on CO_2 corrosion of carbon steel in simulated oil and gas well environments, *Corros. Sci.*, 84(2014), p. 165.

[4] S. Dong, W. Liu, J. Zhang, X.Q. Lin, J. He, and M.X. Lu, Effect of oxygen on CO_2 corrosion and erosion-corrosion behavior of N80 steel under high temperature and high pressure, [in] *NACE International Corrosion Conference Series: Corrosion 2014*, San Orlando, 2014, art. No. 4198.

[5] J. Zhang, X.Q. Lin, S.L. Lu, T.T. Wang, W. Liu, S. Dong, C. Yang, and M.X. Lu, Corrosion behavior and mechanism of N80 steel under high temperature and high pressure CO_2–O_2 coexisting condition, [in] *NACE International Corrosion Conference Series: Corrosion 2013*, Florida, 2013, art. No. 2479.

[6] X. Jiang, Y.G. Zheng, and W. Ke, Effect of flow velocity and entrained sand on inhibition performances of two inhibitors for CO_2 corrosion of N80 steel in 3% NaCl solution, *Corros. Sci.*, 47(2005), No. 11, p. 2636.

[7] P.Y. Wang, J. Wang, S.Q. Zheng, Y.M. Qi, M.X. Xiong, and Y.J. Zheng, Effect of H_2S/CO_2 partial pressure ratio on the tensile properties of X80 pipeline steel, *Int. J. Hydrogen Energy*, 40(2015), No. 35, p. 11925.

[8] L. Wei, X.L. Pang, C. Liu, and K.W. Gao, Formation mechanism and protective property of corrosion product scale on X70 steel under supercritical CO_2 environment, *Corros. Sci.*, 100(2015), p. 404.

[9] G. McIntire, J. Lippert, and J. Yudelson, The effect of dissolved CO_2 and O_2 on the corrosion of iron, *Corrosion*, 46(1990), No. 2, p. 91.

[10] D. John, B. Kinsella, S. Bailey, and R. De Marco, Flow dependence of carbon dioxide corrosion rates and the interference of trace dissolved oxygen, [in] *NACE International Corrosion Conference Series: Corrosion 2007*, Nashville, Tennessee, 2007, art. No. 07315.

[11] C.F. Chen, M.X. Lu, G.X. Zhao, Z.Q. Bai, and W. Chang, The ion passing selectivity of CO_2 corrosion scale on N80 tube steel, [in] *NACE International Corrosion Conference Series: Corrosion 2003*, San Dieg, 2003, art. No. 03342.

[12] C.F. Chen, M.X. Lu, D.B. Sun, Z.H. Zhang, and W. Chang, Effect of chromium on the pitting resistance of oil tube steel in a carbon dioxide corrosion system, *Corrosion*, 61(2005), No. 6, p. 594.

[13] F. Ayello, K. Evans, R. Thodla, and N. Sridhar, Effect of impurities on corrosion of steel in supercritical CO_2, [in] *NACE International Corrosion Conference Series*: *Corrosion 2010*, San Antonio, 2010, art. No. 10193.

[14] Y. Hua, R. Barker, and A. Neville, The effect of O_2 content on the corrosion behavior of X65 and 5Cr in water-containing supercritical CO_2 environments, *Appl. Surf. Sci.*, 356(2015), p. 499.

[15] W. Schulz, D. Huenert, H. Nitschke, R. Saliwan-Neumann, and A. Kranzmann, Comparison of the corrosion behavior of 9–12% Cr steels in H_2O, H_2O–CO_2 and H_2O–CO_2–O_2, [in] *NACE International Corrosion Conference Series: Corrosion 2009*, Atlanta, 2009, art. No. 09264.

[16] T. Hong and M. Nagumo, Effect of surface roughness on early stages of pitting corrosion of Type 301 stainless steel, *Corros. Sci*., 39(1997), No. 9, p. 1665.

[17] A. Shahryari, W. Kamal, and S. Omanovic, The effect of

surface roughness on the efficiency of the cyclic potentiodynamic passivation (CPP) method in the improvement of general and pitting corrosion resistance of 316LVM stainless steel, *Mater. Lett*., 62(2008), No. 23, p. 3906.

[18] American Society for Testing and Materials, *ASTM Standard G31, Practice for Laboratory Immersion Corrosion Testing of Metals*, ASTM International, 2004.

[19] International Standardization Organization, *ISO 8407: Corrosion of Metals and Alloys—Removal of Corrosion Products from Corrosion Test Specimens*, 2010.

[20] S.D. Zhu, G.S. Zhou, J. Miao, R. Cai, and J.F. Wei, Mechanical properties of CO_2 corrosion scale formed at different temperatures and their relationship to corrosion rate, *Corros. Eng. Sci. Technol.*, 47(2012), No. 3, p. 171.

[21] S.Q. Guo, L.N. Xu, L. Zhang, W. Chang, and M.X. Lu, Characterization of corrosion scale formed on 3Cr steel in CO_2-saturated formation water, *Corros. Sci.*, 110(2016), p. 123.

[22] X.G. Zheng and D.J. Young, High-temperature corrosion of Cr_2O_3-forming alloys in CO–CO_2–N_2 atmospheres, *Oxid. Met.*, 42(1994), No. 3, p. 163.